RSC Advances

ROYAL SOCIETY OF CHEMISTRY

www.rsc.org/advances

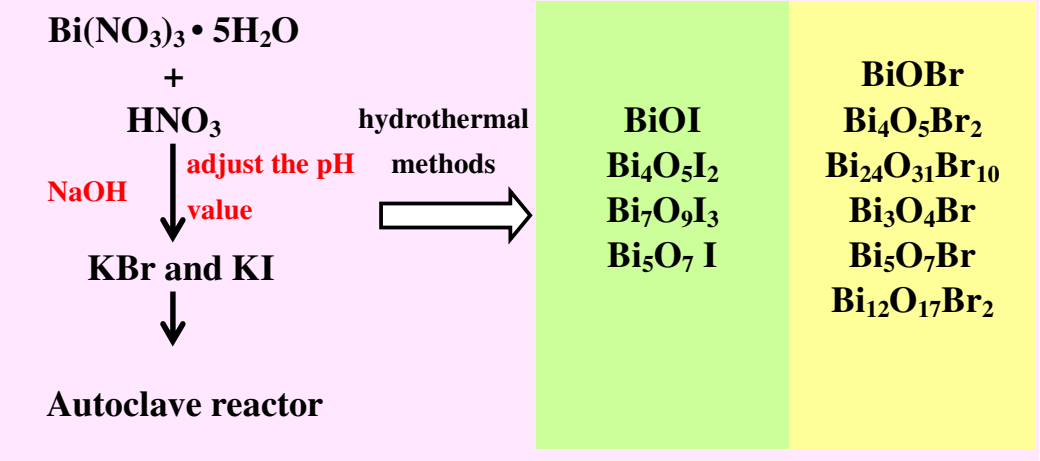

Figure abstract. Schematic diagram of synthesis method for as-prepared BiO_pBr_q/BiO_mI_n under different conditions.

RSC Advances RSCPublishing

PAPER

Hydrothermal Synthesis of Bismuth Oxybromide-Bismuth Oxyiodide Composites with highly visible light Photocatalytic performance for the degradation of CV and Phenol

Yu-Rou Jiang, Shang-Yi Chou, Jia-Lin Chang, Shiuh-Tsuen Huang, Ho-Pan Lin, Chiing-Chang Chen*

Cite this: DOI: 10.1039/xoxxoooooox

Received ooth January 2012,
Accepted ooth January 2012

DOI: 10.1039/xoxxoooooox

www.rsc.org/

This is the first report that a series of BiO_pBr_q/BiO_mI_n heterojunctions are prepared using controlled hydrothermal methods. The compositions and morphologies of the BiO_pBr_q/BiO_mI_n could be controlled by adjusting some growth parameters, including reaction pH value, temperature, time, and KBr/KI molar ratio. The photocatalytic efficiency of powder suspensions was evaluated by measuring Crystal Violet (CV) and phenol concentration. Both the photocatalytic process and the photosensitized process would work concurrently. The quenching effects of various scavengers and EPR indicated that the reactive $O_2^{\bullet-}$ played a major role and •OH and h^+ played a minor role. The photocatalytic activity of BiO_pBr_q/BiO_mI_n heterojunctons reached the maximum rate constant of 0.5285 (or 0.4713) h^{-1}, 10 times higher than that of P25-TiO_2, 14 times higher than that of BiOBr, and 6 times higher than that of BiOI.

1. Introduction

The large amount of dyes used in the dyeing stage of textile manufacturing processes represents an increasing environmental danger due to their refractory carcinogenic nature. Particularly, triphenylmethane (TPM) dyes are consumed heavily in leather, cosmetic, paper, and food industries for the coloring of plastics, oil, fats, waxes, and varnish.[1] The photocytotoxicity of TPM dyes, based on the production of the reactive oxygen species, is intensively studied with the regard of the photodynamic treatment.[2] However, there is a great concern about the thyroid peroxidase-catalyzed oxidation of TPM dyes because the reactions might form various *N*-de-alkylated aromatic amines, whose structures are similar to aromatic amine carcinogens.[3] Cationic TPM dyes are widely used as antimicrobial agents. Recent reports indicated that they might further serve as targetable sensitizers in the photo-destruction of specific cellular components or cells.[2,3] The photocatalysis process has been successfully used for degrading TPM dye pollutants in the past few years.[4,5] In view of the efficient utilization of visible light, the development of new and efficient visible-light-driven photocatalysts remains a major challenge from the practical use and commercial viewpoint.

Recently, the development of visible-light-sensitive photocatalysts has received considerable attention as an alternative of wastewater treatment. An effective and simple strategy to improve the photocatalytic activity of a photocatalyst is the incorporation of a heterostructure (or composites), because heterojunctions (or composites) have great potential for tuning the desired electronic properties of composite photocatalysts and efficiently separating the photogenerated electron–hole pairs.[6-12] In recent years, as a new family of promising photocatalysts, bismuth oxyhalides,[13-16] which belongs to V-VI-VII family of the multi-component metal oxyhalides, have demonstrated remarkable photocatalytic activities due to their uniquely layered structures with an internal static electric field perpendicular to each layer, which can induce effective separation of photogenerated electron-hole pairs. An effective and simple tactic to improve the photocatalytic activity of a photocatalyst is the architecture of a heterostructure, as the heterojunction has great potential in tuning the desired electronic properties of the composite photocatalysts and efficiently separating the photogenerated electron-hole pairs.[17] Xiao *et al.* [18] reported the synthesis of BiOI/BiOCl phases exhibiting high photocatalytic activities under visible light irradiation for the degradation of bisphenol-A and

methyl orange, respectively. Cao *et al.* [19] developed a facile synthesis of BiOCl/BiOI by a sol-gel process.

This research reports the preparation and characterization of a series of BiO_pBr_q/BiO_mI_n photocatalysts. This is the first presence demonstrating the systemic synthesis study on BiO_pBr_q/BiO_mI_n photocatalysts by autoclave hydrothermal methods. The photocatalytic activities of BiO_pBr_q/BiO_mI_n are evaluated by measuring the degradation rate of CV and phenol has an excellent activity under visible light irradiation. In comparison to P25-TiO_2, the new photoactive material demonstrates higher rate in removing aqueous CV under visible light irradiation.

2. Experiment

2.1 Materials

The purchased $Bi(NO_3)_3$•$5H_2O$, KI (Katayama), KBr (Shimakyu), CV dye (TCI), *p*-benzoquinone (Alfa aesar), sodium azide (Sigma), ammonium oxalate (Osaka), and isopropanol (Merck) were obtained and used without any further purification. Reagent-grade sodium hydroxide, nitric acid, ammonium acetate and HPLC-grade methanol were obtained from Merck.

2.2 Synthesis of BiO_pBr_q/BiO_mI_n

5 mmol Bi $(NO_3)_3$•$5H_2O$ was first mixed in a 50 mL flask, and followed by adding 5 mL 4M HNO_3. With continuous stirring, 2 M NaOH was added dropwised to adjust the pH value; and when a precipitate was formed, 2 mL KBr and KI was also added dropwised. The solution was then stirred vigorously for 30 min and transferred into a 30 mL Teflon-lined autoclave, which was heated up to 110–260 ^oC for 12h and then naturally cooled down to room temperature. The resulting solid precipitate was collected by filtration, washed with deionized water and methanol to remove any possible ionic species in the solid precipitate, and then dried at 60^oC overnight. Depending on the molar ratio of KBr to KI (2:1, 1:2), pH value, temperatures, and time, different BiO_pBr_q/BiO_mI_n composites could be synthesized and labeled as in Table S1 of supplementary materials, namely BB1I2-1-110-12 (Br:I = 1:2; pH = 1; temp = 110 ^oC; time = 12h) to BB2I1-13-260-12 (Br:I = 2: 1; pH = 13; temp = 260 ^oC; time = 12h) for as-prepared samples, respectively.

2.3 Instruments and Analytical Methods

The products were characterized using XRD, FE-SEM-EDS, HRXPS, FE-TEM-EDS, CL, EPR, and BET. The intermediates formed during the decomposition process were isolated, identified, and characterized using HPLC-PDA-ESI-MS. The detailed conditions are described in the supplementary materials.

2.4 Photocatalytic activity test

The aqueous suspension of CV (100 mL, 10 ppm) and the amount of catalyst powder were placed in the Pyrex flask. The pH value of the suspension was adjusted by adding either NaOH or HNO_3 solution. Prior to irradiation, the suspension was magnetically stirred in the dark for ca. 30 min to establish adsorption/desorption equilibrium between the dye and the surface of the catalyst under ambient air-equilibrated conditions. The irradiation was carried out using visible-light lamps (150 W Xe arc). The light intensity was fixed on 32.1 Wm^{-2} when the reactor was placed 30 cm away from the light source. The irradiation experiments of CV were carried out on stirring aqueous solution contained in a 100mL flask. At the given irradiation time intervals, 5 mL aliquot was collected and centrifuged to remove the catalyst. The supernatant was analyzed by HPLC-ESI-MS after readjusting the chromatographic conditions in order to make the mobile phase compatible with the working conditions of the mass spectrometer.

3. Results and discussion

3.1 Phase structure

Fig. 1 and Fig. S1-S7 (ESI†) show the XRD patterns of the as-prepared BiO_pBr_q/BiO_mI_n samples. The XRD patterns clearly reveal the coexistence of the different phases. All the as-prepared BiO_pBr_q/BiO_mI_n samples using the hydrothermal method described at different temperatures and pH are the BiOBr (JCPDS 09-0393), $Bi_4O_5Br_2$ (JCPDS 37-0669), $Bi_{24}O_{31}Br_{10}$ (JCPDS 75-0888), Bi_3O_4Br (JCPDS 84-0793), Bi_5O_7Br (JCPDS 38-0493), $Bi_{12}O_{17}Br_2$ (JCPDS 37-0701), BiOI (JCPDS 73-2062), $Bi_7O_9I_3$, [20, 21] and Bi_5O_7I (JCPDS 40-0548) phases. The XRD patterns for pH= 1, 4, 7, 10, and 13 are identical to those reported for BiOI single phase, BiOBr/BiOI, $Bi_3O_4Br/Bi_7O_9I_3$, Bi_5O_7Br/Bi_5O_7I, $Bi_{24}O_{31}Br_{10}$/BiOI, Bi_3O_4Br/Bi_5O_7I binary phase, and BiOBr/$Bi_{24}O_{31}Br_{10}$/BiOI, BiOBr/$Bi_4O_5Br_2$/BiOI ternary phases. Table 1 summarizes the results of the XRD measurements.

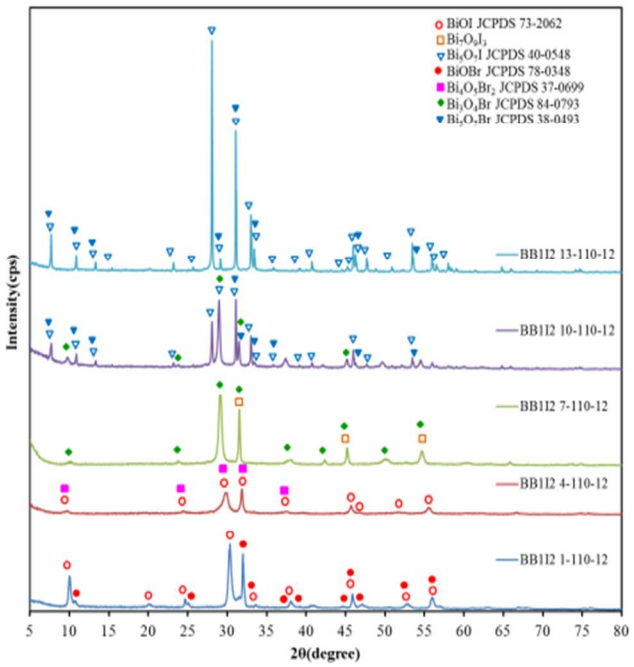

Fig. 1 (a) XRD patterns of as-prepared BiO_pBr_q/BiO_mI_n samples under different pH values. (Molar ratio KBr/KI =1/2, hydrothermal conditions: temp = 110°C, pH = 1-13, time = 12 h)

Fig. 2-4 display that BB1I2-4-210-12, BB2I1-4-110-12, and BB1I2-4-110-12 are composed of sheets or plates with different sizes, consistent with the TEM observation. In addition, the EDS spectrum shows the sample including Bi, O, Br and I elements. The TEM-EDS results show that the main elements of these samples are bismuth, iodine, chlorine, and oxygen. The Br (or I) atomic ratio (%) of the samples is within the range of 3.86-7.83 (or 9.55-15.37), corresponding to different heterojunctions. The HRTEM image reveals that two sets of different lattice images are found with the d spacing of 0.2824 and 0.3012 nm, corresponding to the (4 0 2) plane of $Bi_4O_5Br_2$ and the (1 0 2) plane of BiOI (Fig. 2), 0.2814 and 0.2824 nm, corresponding to the (0 2 0) plane of $Bi_4O_5Br_2$ and the (1 1 0) plane of BiOI (Fig 3), and 0.2836 and 0.2812 nm, corresponding to the (1 2 0) plane of $Bi_4O_5Br_2$ and the (1 1 0) plane of BiOI (Fig. 4), respectively, which is in good accordance with the results of the XRD patterns. The results suggest that the $Bi_4O_5Br/BiOI$ composites have been formed in the composites, which will favor for the separation of photoinduced carriers and thus acquire high photocatalytic activities.

Table 1 Crystalline phase changes of binary bismuth oxyhalides nanosheets prepared under different reaction conditions.(● $BiOBr$; ■ $Bi_4O_5Br_2$; ▲ $Bi_{24}O_{31}Br_{10}$; ◆ Bi_3O_4Br; ● $Bi_{12}O_{17}Br_2$; ▼ Bi_5O_7Br; ○ $BiOI$; □ $Bi_7O_9I_3$; ▽ Bi_5O_7I)

pH	Temp (°C)			
	110	160	210	260
BB1I2				
1	■○	■○	■○	■○
4	■○	■○	■○	■▲○
7	◆□	◆□	◆□	◆□
10	▼▽	▼▽	◆▽	▼▽
13	▼▽	▼▽	▼▽	▼▽
BB2I1				
pH	Temp (°C)			
	110	160	210	260
1	●○	●○	●○	●
4	■○	■○	■▲○	■▲○
7	●■○	●■○	▲○	▲○
10	◆▽	◆▽	◆▽	◆▽
13	▼▽	▼▽	▼▽	▼▽

In this experiment, pH values play a major role in controlling the composition and anisotropic growth of crystals. The results show that a series of changes in the compounds occur at different pH values of hydrothermal reactions, described as BiOBr → $Bi_4O_5Br_2$ → $Bi_{24}O_{31}Br_{10}$ → Bi_3O_4Br → Bi_5O_7Br → $Bi_{12}O_{17}Br_2$ → α-Bi_2O_3 and BiOI → $Bi_4O_5I_2$ → $Bi_7O_9I_3$ → Bi_3O_4I → Bi_5O_7I → α-Bi_2O_3. The possible processes for the formation of BiO_pBr_q/BiO_mI_n samples are described as follows [Eqs. (1) – (18)].

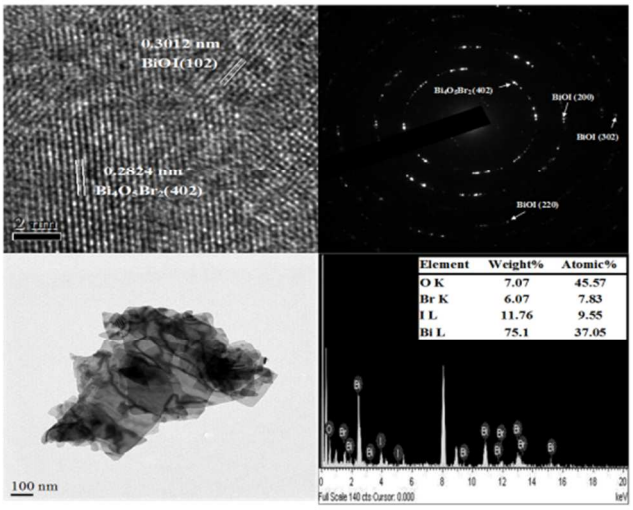

Fig. 2 FE-TEM images and EDS of BB1I2-4-210-12 sample by the hydrothermal autoclave method.

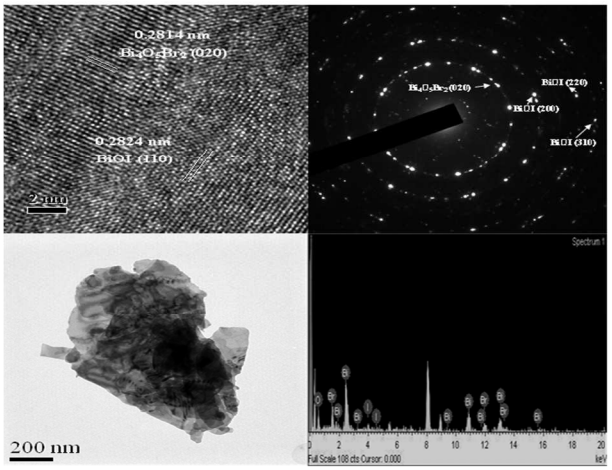

Fig. 3 FE-TEM images and EDS of BB2I1-4-110-12 sample by the hydrothermal autoclave method.

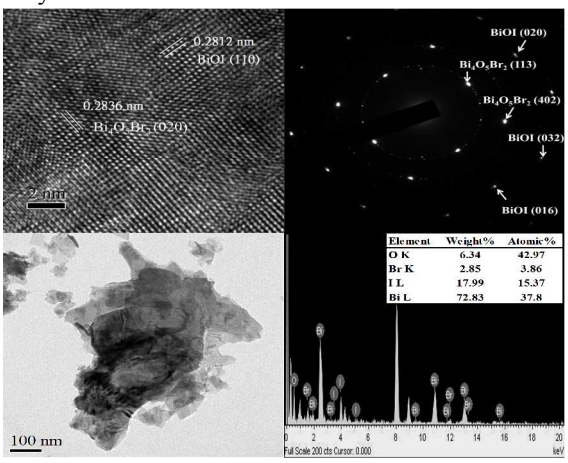

Fig. 4 FE-TEM images and EDS of BB1I2-4-110-12 sample by the hydrothermal autoclave method.

$$Bi^{3+} + 3OH^- \rightarrow Bi(OH)_{3(s)} \quad (1)$$

$$2Bi(OH)_{3(s)} + Br^- \rightarrow BiOBr_{(s)} + H_2O + OH^- \quad (2)$$

$$Bi^{3+} + 3Br^- \rightarrow BiBr_{3\,(s)} \quad (3)$$

$$BiBr_{3\,(s)} + 2OH^- \rightarrow BiOBr_{(s)} + 2Br^- + H_2O \quad (4)$$

$$4BiOBr_{(s)} + 2OH^- \rightarrow Bi_4O_5Br_{2(s)} + 2Br^- + H_2O \quad (5)$$

$$6Bi_4O_5Br_{2(s)} + 2OH^- \rightarrow Bi_{24}O_{31}Br_{10(s)} + 2Br^- + H_2O \quad (6)$$

$$Bi_{24}O_{31}Br_{10(s)} + 2OH^- \rightarrow 8Bi_3O_4Br_{(s)} + 2Br^- + H_2O \quad (7)$$

$$5Bi_3O_4Br_{(s)} + 2OH^- \rightarrow 3Bi_5O_7Br_{(s)} + 2Br^- + H_2O \quad (8)$$

$$12Bi_5O_7Br_{(s)} + 2OH^- \rightarrow 5Bi_{12}O_{17}Br_{2\,(s)} + 2Br^- + H_2O \quad (9)$$

$$Bi_{12}O_{17}Br_{2(s)} + 2OH^- \rightarrow 6Bi_2O_{3(s)} + 2Br^- + H_2O \quad (10)$$

$$2Bi(OH)_{3(s)} + I^- \rightarrow BiOI_{(s)} + H_2O + OH^- \quad (11)$$

$$Bi^{3+} + 3^- \rightarrow BiI_{3\,(s)} \quad (12)$$

$$BiI_{3(s)} + 2OH^- \rightarrow BiOI_{(s)} + 2I^- + H_2O \quad (13)$$

$$4BiOI_{(s)} + 2OH^- \rightarrow Bi_4O_5I_{2(s)} + 2I^- + H_2O \quad (14)$$

$$7Bi_4O_5I_{2(s)} + 2OH^- \rightarrow 4Bi_7O_9I_{3(s)} + 2I^- + H_2O \quad (15)$$

$$3Bi_7O_9I_{3(s)} + 2OH^- \rightarrow 7Bi_3O_4I_{(s)} + 2I^- + H_2O \quad (16)$$

$$5Bi_3O_4I_{(s)} + 2OH^- \rightarrow 3Bi_5O_7I_{(s)} + 2I^- + H_2O \quad (17)$$

$$2Bi_5O_7I_{(s)} + 2OH^- \rightarrow 5Bi_2O_{3(s)} + 2I^- + H_2O \quad (18)$$

These equations show that BiOBr (or BiOI) is formed at the beginning of the reaction, and then OH^- gradually substitutes Br^- (or I^-) in the basic conditions, resulting in the reduced content of Br^- (or I^-) in the products. Increasing pH could gradually obtain BiOBr, $Bi_4O_5Br_2$, $Bi_{24}O_{31}Br_{10}$, Bi_3O_4Br, Bi_5O_7Br, $Bi_{12}O_{17}Br_2$, and BiOI, $Bi_4O_5I_2$, $Bi_7O_9I_3$, Bi_3O_4I, Bi_5O_7I, and α-Bi_2O_3. The higher pH value reveals the lower Br^- (or I^-) content in the products, until the content of Br^- (or I^-) in the products is fully replaced by OH^-, finally resulting in the formation of α-Bi_2O_3 under strong basic conditions. A competitive relationship typically exists among OH^-, Br^-, and I^- ions in the aqueous solution. It is demonstrated that a different BiO_pBr_q/BiO_mI_n can be selectively prepared through adjusting pH values under the

Table 2 Physical and chemical properties of BiO_pBr_q/BiO_mI_n.

Catalyst code	EDS of atomic ratio(%)				XPS of atomic ratio(%)				E_g (eV)
	Bi	O	Br	I	Bi	O	Br	I	
BB1I2-1-110-12	31.64	39.72	11.04	17.59	70.9	16.3	8.8	3.9	1.58
BB1I2-4-110-12	25.35	54.35	7.52	12.78	89.2	5.1	2.4	3.3	1.80
BB1I2-7-110-12	33.80	52.00	2.77	11.43	88.8	9.0	0.8	1.4	1.97
BB1I2-10-110-12	31.29	59.85	1.11	7.75	85.2	11.9	0.8	2.1	2.18
BB1I2-13-110-12	36.25	57.06	0.06	6.63	59.2	37.0	0.4	3.5	2.56
BB2I1-1-110-12	24.03	48.33	19.21	8.44	77.8	12.6	8.4	1.2	1.68
BB2I1-4-110-12	31.22	48.18	13.30	7.30	81.7	11.5	5.0	1.7	1.90
BB2I1-7-110-12	30.23	50.52	12.97	6.27	79.0	15.4	4.8	0.9	1.83
BB2I1-10-110-12	33.49	55.41	5.58	5.52	72.2	22.9	3.2	1.7	2.16
BB2I1-13-110-12	32.80	58.33	1.23	7.64	65.9	31.1	2.4	0.5	2.38
BB3-1-110-12	28.54	45.45	26.00	-	59.5	22.0	18.5	-	2.61
BI3-1-110-12	24.47	50.22	-	25.31	80.3	11.9	-	7.8	1.59

hydrothermal method.

3.2 Morphological structure and Composition

The surface morphology of the BiO_pBr_q/BiO_mI_n is examined by FE-SEM-EDS (Fig. S8-S9, ESI†). From Table 2, the EDS results show that the main elements of these samples are bismuth, bromine, iodine, and oxygen under different pH values. The detailed morphological structure and composition are described in the supplementary materials.

3.3 XPS analysis

XPS is employed to examining the purity of the prepared BiO_pBr_q/BiO_mI_n products, and the spectra are shown in Fig. 5-6. Fig. 5 shows the total survey spectra of Bi 4f, Br 3d, I 3d, and O1s XPS of the five BiO_pBr_q/BiO_mI_n samples. According to the Fig. 5(a), the observation of transition peaks involving in the Bi 4f, Br 3d, I 3d, O 1s, and C 1s orbitals reveals that the catalysts are constituted by the elements of Bi, O, Br, I, and C. The characteristic binding energy value of 158.1-158.9 eV for Bi $4f_{7/2}$ (Fig. 5(b)) reveals a trivalent oxidation state for bismuth. An additional spin–orbit doublet with the binding energy of 155.7-156.3 eV for Bi $4f_{7/2}$ is also observed in all samples, suggesting that certain parts of bismuth exist in the (+3-x) valence state. This indicates that the trivalent bismuth partially reduces to the lower valence state by the hydrothermal autoclave method. A similar chemical shift of approximately 2.4-2.6 eV for Bi $4f_{7/2}$ was also observed by Chen *et al.*[5] They concluded that $Bi^{(+3-x)}$ formal oxidation state could most probably be attributed to the substoichiometric forms of Bi within the Bi_2O_2 layer and the formation of low oxidation state resulted in oxygen vacancy in the crystal lattice. However, it was assumed that $Bi^{(+3-x)}$ formal oxidation state could most likely be attributed to the substoichiometric forms of Bi at the outer site of the particles and the formation of low oxidation state resulted in oxygen vacancy in the crystal surface. Fig. 5(c) shows the high-resolution XPS spectra for the O 1s region, which can be fitted into two peaks. The main peak at 529.1 eV is attributed to the Bi-O bonds in $(Bi_2O_2)^{2+}$ slabs of BiOX layered structure, and the peak at 530.9 eV is assigned to the hydroxyl groups on the surface.[15] From Fig. 5(d), the binding energy of 67.4-67.8 eV and 68.5-68.9 eV is referred to the Br $3d_{5/2}$ and $3d_{3/2}$ respectively which can be assigned to Br at the monovalent oxidation state. The binding energy of 617.8-618.7 eV and 629.5-630.2eV is referred to I $3d_{5/2}$ and $3d_{3/2}$ respectively which can be assigned to I at the monovalent oxidation state (Fig. 5(e)). In the Bi_2O_3 (BB3-1-110-12 (BiOBr) or BI3-1-110-12 (BiOI)) samples, two sets of peaks centered at 164.0 and 158.5 (164.2 and 158.7 or 163.5 and 158.1) eV can be attributed to Bi $4f_{5/2}$ and Bi $4f_{7/2}$, demonstrating that the main chemical states of the bismuth element in the samples is trivalent. The characteristic binding energy reveals a trivalent oxidation state for the Bi^{+3}–O (Bi^{+3}–Br or Bi^{+3}–I) bonding. Two additional spin–orbit doublet with the binding energy for Bi $4f_{7/2}$ is also observed, suggesting that certain parts of bismuth exist in the Bi^{+3-x}–O (Bi^{+3-x}–Br or Bi^{+3-x}–I) bonding.[5] The XPS result reveals that the possible processes for the formation of bismuth oxybromoiodides are described as Eqs 1-18, which are consistent with the previous result by XRD and TEM analyses. Besides, the results show that the main elements of these samples are bismuth, bromine, iodine, and oxygen from **Table 2**. The Br (or I) atomic ratio (%) of the samples is within the range of 0.4-8.8 (or 0.5-3.9), corresponding to different BiO_pBr_q/BiO_mI_n composites.

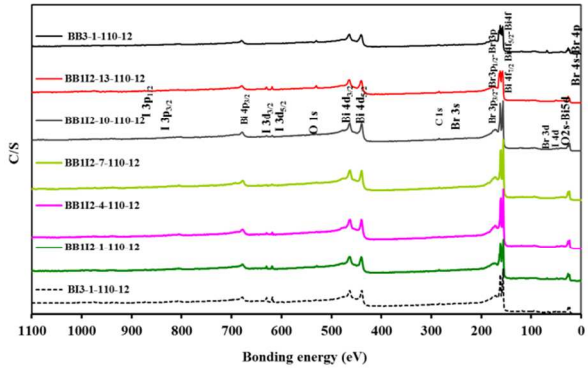

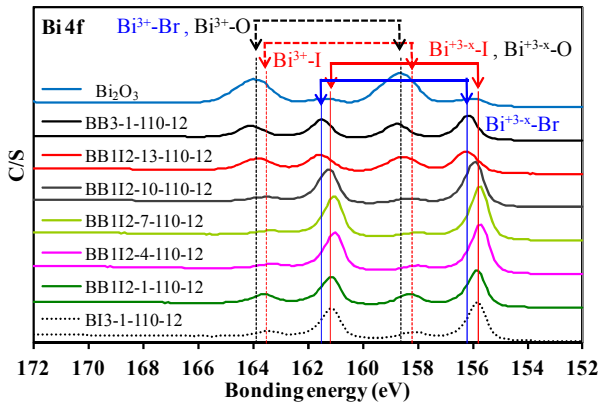

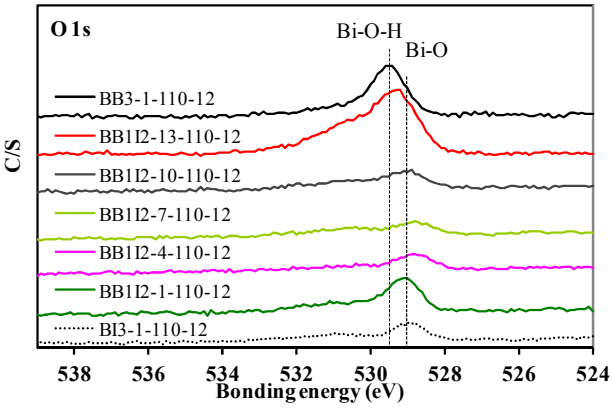

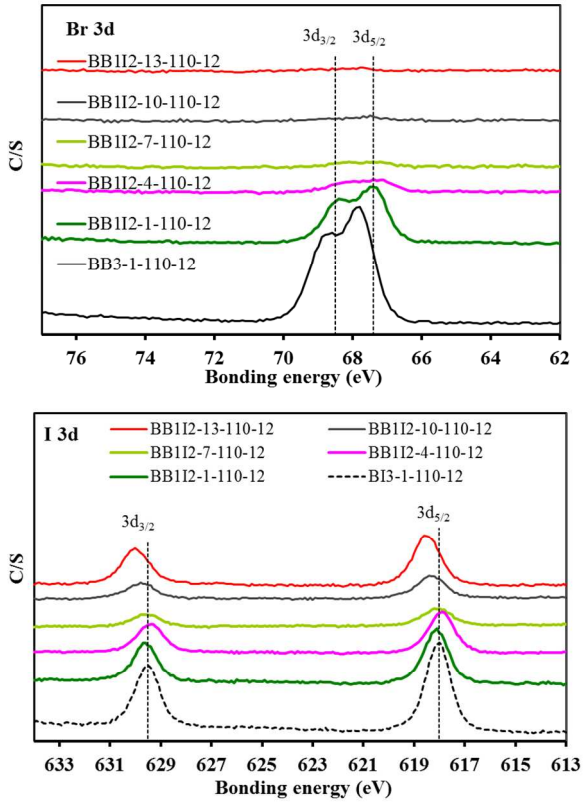

Fig. 5. High resolution XPS spectra of as-prepared BiO_pBr_q/BiO_mI_n samples under different pH values. (a) total survey; (b) Bi 4f; (c) O 1s; (d) Br 3d; (e) I 3d. (Molar ratio KBr/KI = 1/2)

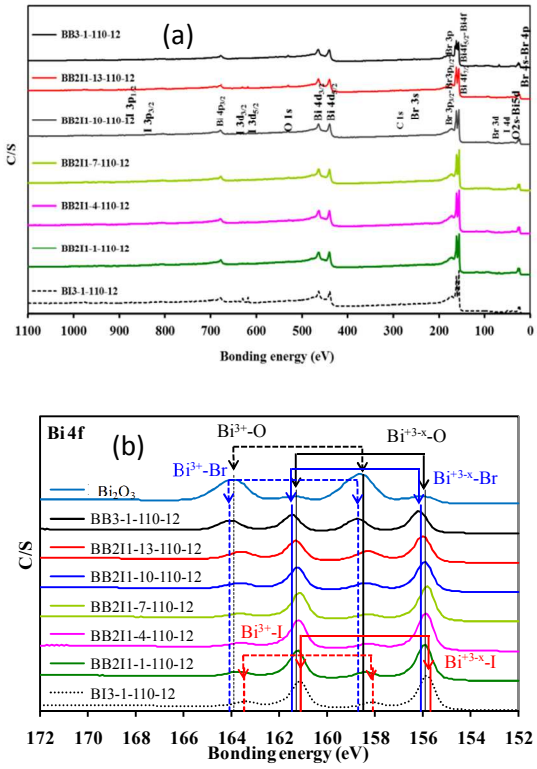

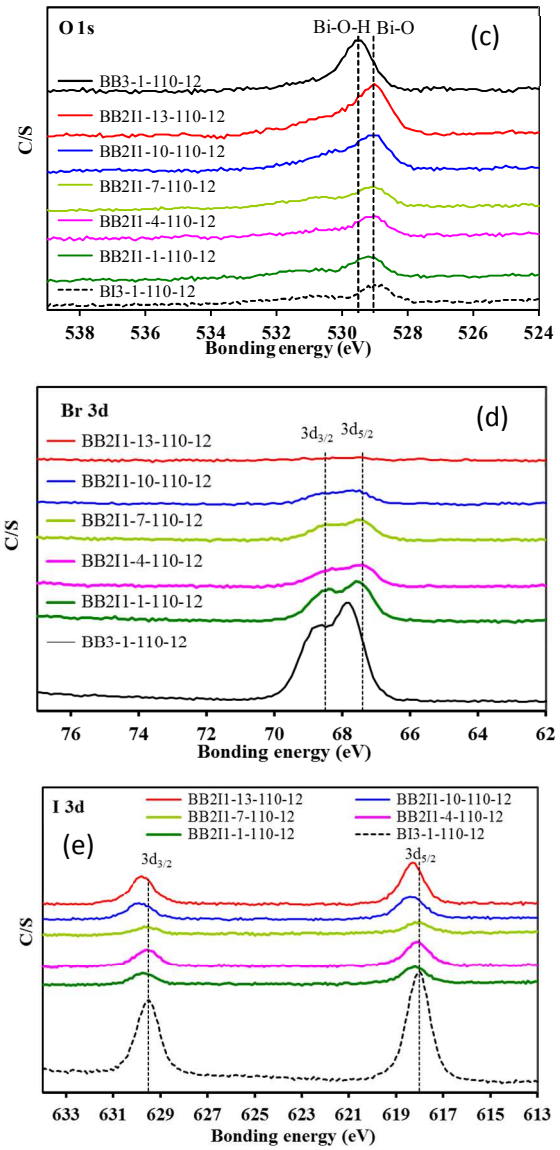

Fig. 6. High resolution XPS spectra of as-prepared BiO_pBr_q/BiO_mI_n samples under different pH values. (a) total survey; (b) Bi 4f; (c) O 1s; (d) Br 3d; (e) I 3d. (Molar ratio KBr/KI = 2/1)

3.4 Photophysical properties of the new photocatalysts

UV–vis diffuse reflectance spectra of different catalysts are shown in Fig. 7 (a). It can be observed that BiOBr absorbs visible light slightly while the absorption edge of BiOI extends to the whole spectra of visible light. Moreover, the absorption edges of BiO_pBr_q/BiO_mI_n composites have a monotonic red shift response of BiO_pBr_q. Base on their absorption spectra, E_g of the semiconductor can be calculated from the $\alpha h\upsilon = A(h\upsilon - E_g)^{n/2}$ equation.[19,22] The values of n for BiOBr and BiOI are 4 and 4, respectively. E_g of BiO_pBr_q/BiO_mI_n is determined from a plot of $(\alpha h\upsilon)^{1/2}$ vs energy ($h\upsilon$) in Fig. 7 (b) and elicited to be 1.58-2.56 eV in

Table 2. The difference of band gap energy in the as-prepared BiO_pBr_q/BiO_mI_n can be ascribed to their individual composition with various characteristics. The steep shape and strong absorption in the visible region ascribe the visible light absorption to the intrinsic band gap transition between the valence band and the conduction band, rather than the transition from the impurity levels.[22]

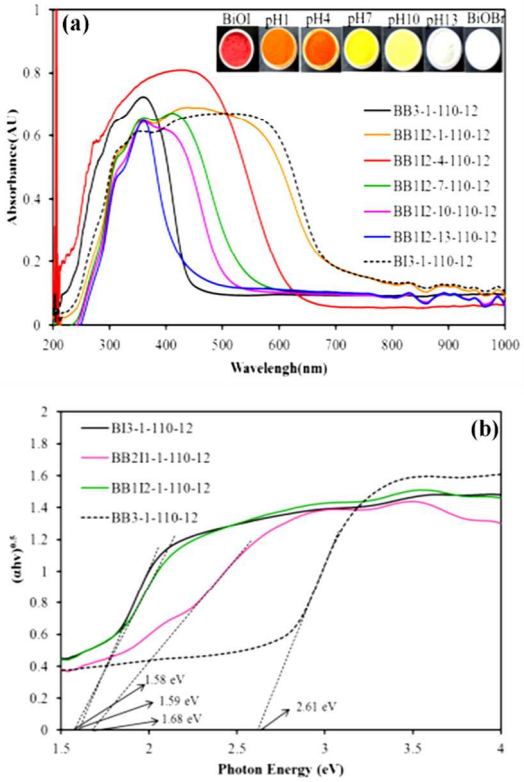

Fig. 7 UV–vis absorption spectra of as-prepared BiO_xCl_y/BiO_mBr_n samples under different (a) pH values and (b) molar ratio.

3.5 Specific surface areas and pore structure

Fig. S10 (a) of ESI† shows the nitrogen adsorption-desorption isotherm curves of BiO_pBr_q/BiO_mI_n samples in different pH values. The isotherm of all samples are close to Type IV (Brunauer-Deming-Deming-Teller, BDDT, classification) with a hysteresis loop at highly relative pressure between 0.6 and 1.0.[23] From Fig. S10 (b) of ESI†, the shape of the hysteresis loop is close to Type H3, suggesting the existence of slit-like pores generally formed by the aggregation of plate-like particles, which is consistent with the self-assembled nanoplate-like morphology of samples. [23]

In Table S2 of ESI†, BB1I2-4-110-12 and BB2I1-4-110-12 have also the larger BET and the pore volume. Thus, the large BET and pore volume of BiO_pBr_q/BiO_mI_n composites may play a role in enhancing the photocatalytic activity. The detailed BET and pore structure are described in the supplementary materials.

Table 3 The pseudo-first-order rate constants for the degradation of CV with BiO_pBr_q/BiO_mI_n photocatalysts under visible light irradiation.

BB1I2 series								
pH	Temp (°C)							
	110		160		210		260	
	$k(h^{-1})$	R^2	$k(h^{-1})$	R^2	$k(h^{-1})$	R^2	$k(h^{-1})$	R^2
1	0.171	0.96	0.137	0.95	0.185	0.96	0.100	0.97
4	0.374	0.95	0.323	0.96	0.528	0.99	0.239	0.99
7	0.064	0.97	0.126	0.99	0.080	0.96	0.106	0.96
10	0.129	0.97	0.201	0.95	0.077	0.95	0.189	0.96
13	0.013	0.96	0.029	0.97	0.042	0.96	0.022	0.96
BB2I1 series								
pH	Temp (°C)							
	110		160		210		260	
	$k(h^{-1})$	R^2	$k(h^{-1})$	R^2	$k(h^{-1})$	R^2	$k(h^{-1})$	R^2
1	0.143	0.97	0.139	0.96	0.249	0.96	0.025	0.98
4	0.471	0.96	0.427	0.96	0.416	0.97	0.310	0.98
7	0.243	0.97	0.398	0.96	0.103	0.97	0.086	0.98
10	0.143	0.96	0.094	0.96	0.087	0.98	0.064	0.93
13	0.009	0.97	0.002	0.98	0.010	0.98	0.020	0.94

BiOBr		BiOI		TiO_2	
$k(h^{-1})$	R^2	$k(h^{-1})$	R^2	$k(h^{-1})$	R^2
0.037	0.97	0.093	0.99	0.057	0.99

3.6 Photocatalytic activity

The changes of the UV-vis spectra during the photodegradation process of CV and phenol in the aqueous BiO_pBr_q/BiO_mI_n dispersions under visible light irradiation are illustrated in Fig. S12 of ESI†. The degradation efficiency as a function of reaction time is illustrated in Fig. S13 of ESI†. The removal efficiency is enhanced significantly in the presence of BiO_pBr_q/BiO_mI_n catalysts. After 48h irradiation, BiO_pBr_q/BiO_mI_n shows superior photocatalytic performance, with CV removal efficiency up to 99%. To further understand the reaction kinetics of CV degradation, the apparent pseudo-first-order model [24] expressed by the $\ln(C_o/C) = k_{app}t$ equation is applied in this experiments. Via the first-order linear fit from the data of Fig. S13 shown in Table 3, k_{app} of BB1I2-4-110-12 is obtained at the maximal degradation rate of 5.285×10^{-1} h^{-1}, greatly higher than the others composites. Therefore, the $Bi_4O_5Br_2$/BiOI composite shows the best photocatalytic activity. The result shows that the $Bi_4O_5Br_2$/BiOI composite is a much more effective photocatalyst than the others. The superior photocatalytic ability of BiO_pBr_q/BiO_mI_n may be ascribed to its efficient utilization of visible light and the high separation efficiency of the electron-hole pairs with its composites.

The durability of the $Bi_4O_5Br_2$/BiOI (BB1I2-4-210-12) composite is evaluated through the recycle of the used catalyst. There is no apparent loss of photocatalytic activity in

removing crystal violet in the fifth cycle, and even in the tenth run, the declination in photocatalytic activities is less than 3% (Fig. 8 (a)). The used $Bi_4O_5Br_2$/BiOI is also examined by XRD, and there is no detectable difference between the as-prepared and used samples (Fig. 8 (b)). Therefore, it can be deduced that the $Bi_4O_5Br_2$/BiOI composite has good photostability.

3.7 Cathodoluminescence spectrum

To investigate the separation capacity of photogenerated carriers in heterostructures, the CL spectra of BiOBr, BiOI, and BiO_pBr_q/BiO_mI_n are measured and the results are given in Fig. 9 The characteristic emission peak around 2.01 eV nearly disappears for the BiO_pBr_q/BiO_mI_n heterostructure, indicating that the recombination of photogenerated charge carriers is inhibited greatly. The efficient charge separation could increase the lifetime of charge carriers and enhance the efficiency of interfacial charge transfer to adsorbed substrates, and then improve the photocatalytic activity.

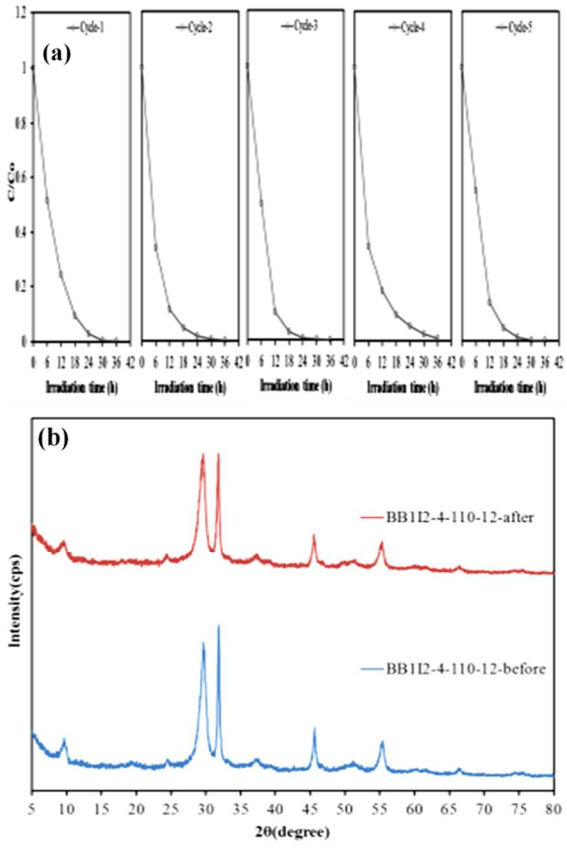

Fig. 8 (a) Cycling runs and (b) XRD patterns acquired before and after in the photocatalytic degradation of CV in the presence of BB1I2-4-110-12.

3.8 Separation and Identification

With visible irradiation, temporal variations occurring in the solution of CV dye during the degradation process is examined by HPLC-PDA-MS. Given the CV irradiation up to 24 h at pH 4, the chromatograms are illustrated in Fig. S14 of supplementary materials and recorded at 580, 350, and 300 nm, and nineteen intermediates are identified, with the retention time under 50 min. The CV dye and its related intermediates are denoted as species A-J, a-f, and α-γ. Except for the initial CV dye (peak A), the peaks initially increase before subsequently decreasing, indicating the formation and transformation of the intermediates.

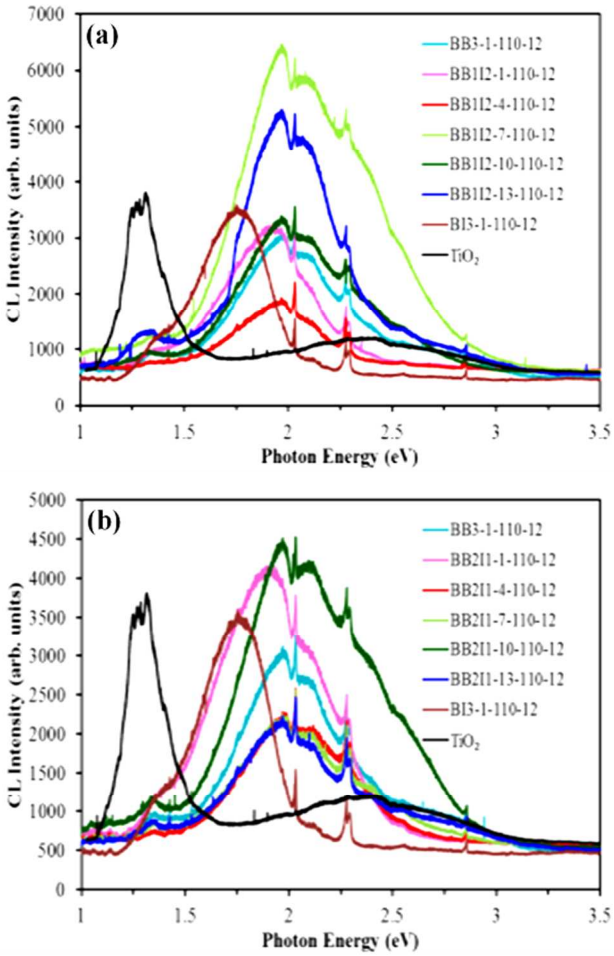

Fig. 9 Photoluminescence spectra of TiO_2, BiOBr, BiOI, and BiO_xCl_y/BiO_mBr_n. Molar ratio KBr/KI (a) 1/2, (b) 2/1.

In Fig. S15 of ESI†, the maximum absorption of the spectral bands shifts from 588.5 nm (spectrum A) to 541.5 nm (spectrum J), from 377.0 nm (spectrum a) to 339.0 nm (spectrum f), and from 309.1 nm (spectrum α) to 278.3 nm (spectrum γ). The maximum adsorption in the visible and ultraviolet spectral region of each intermediate is depicted in Table S3. They are identified as A-J a-f, and α-γ, respectively corresponding to the peaks A-J, a-f, and α-γ in Fig. S14

(ESI†). These shifts of the absorption band are presumed to result from the formation of a series of *N*-de-methylated intermediates. From these results, several families of intermediates could be distinguished. The intermediates are further identified using the HPLC-ESI mass spectrometric method, and the relevant mass spectra are illustrated in Fig. S16 and Table S3 (ESI†). The molecular ion peaks appear in the acid forms of the intermediates. The detailed data of intermediates are described in the supplementary information.

3.9 Mechanism of photocatalytic degradation CV

Generally speaking, three possible reaction mechanisms are suspected to be involved in the dye photodegradation by a semiconductor, namely (i) photolysis process, (ii) dye photosensitization process, and (iii) photocatalytic process.[25] In this experiment, CV degradation by the photolysis process upon visible light in the blank experiment is not observable.

In this study, slight changes in the CV concentration over different samples can be detected in 30 min of dark adsorption experiment before the photocatalytic reactions. The slight CV adsorptions on the catalyst benefits the transfer of charge carriers between the dye and the catalyst surfaces in the dye photosensitization process. Presuming that the photosensitization processes take place with BiO_pBr_q/BiO_mI_n, that is to say, the photosensitization mechanism in the CV decomposition is not also neglectable.

As being known, various primary reactive species, such as hydroxyl radical $HO^{\bullet}$, photogenerated hole h^+, superoxide radical $O_2^{-\bullet}$ and singlet oxygen $^1O_2$, can be formed during the photocatalytic degradation process in the UV-vis/semiconductor system.[6,7,26,27] Shenawi-Khalil and his coworkers showed that the Rhodamine-B photodegradation by $yBiO(Br_xI_{1-x})$–(1−y) bismuth oxide hydrate under visible light was dominated by $O_2^{-\bullet}$ and h^+ oxidation being the main active species.[25] Chen *et al.* proposed the pathway for generating active oxygen radicals ($^{\bullet}OH$) on the surface of $Bi_2O_2CO_3$/BiOI for the degradation of dye.[28] Xiao's group revealed that highly efficient visible light driven bisphenol-A removal with BiOBr/BiOI could be attributed to effective separation and transfer of photoinduced charge carriers in BiOBr/BiOI with narrower band gap and more negative conduction band position, which favored the photogenerated holes.[23] Wang *et al.* reported that $^{\bullet}OH$ radicals were generated by multistep reduction $O_2^{-\bullet}$.[29] Therefore, photogenerated holes on the surface of bismuth oxyhalides were not expected to react with OH^-/H_2O to form $^{\bullet}OH$, suggesting that the decomposition of bisphenol-A[18] and Rhodamine [27] could be attributed to a direct reaction with the photogenerated holes or with superoxide radical or both species.

In order to evaluate the effect of the active species during the photocatalytic reaction, a series of quenchers are introduced to scavenge the relevant active species. $O_2^{-\bullet}$, $^{\bullet}OH$, h^+, and $^1O_2$ are investigated by adding 1.0 mM benzoquinone,[30] isopropanol,[31] ammonium oxalate,[32] and sodium azide,[33] respectively. As shown in Fig. 10a, the degradation efficiency of IPA quenching decreased more than that of AO, and the degradation efficiency of BQ quenching decreased more than that of IPA, but the photocatalytic degradation of CV was not affected by the addition of SA. In short, the quenching effects of various scavengers showed that the reactive $O_2^{-\bullet}$ played a major role, and $^{\bullet}OH$ or h^+ played a minor role in CV degradation. From **Fig. 10b**, the six characteristic peaks of the DMPO-O_2^- adducts were observed in visible light irradiated BiO_xCl_y/BiO_mI_n dispersion. But, the four characteristic peaks of DMPO-OH adducts (1:2:2:1 quartet pattern) were not observed in visible light irradiated BiO_xCl_y/BiO_mI_n aqueous dispersion. **Fig. 10b** indicated that no EPR signals were observed when the reaction was performed in the dark, while the signals with intensity of corresponding to the characteristic peak of DMPO-O_2^- adducts[34] were observed during the reaction process under visible light irradiation, and the intensity gradually increased with the prolonged reaction time, suggesting that the $O_2^{-\bullet}$ (major active species) has been formed in presence of BiO_xCl_y/BiO_mI_n and oxygen under visible light irradiation.

Wang *et al.* reported that $^{\bullet}OH$ radicals were generated by multistep reduction $O_2^{-\bullet}$.[29] However, photogenerated holes on the surface of bismuth oxyhalides were not expected to react with OH^-/H_2O to form $^{\bullet}OH$, suggesting that the decomposition of bisphenol-A[18] and Rhodamine [27] could be attributed to a direct reaction with the photogenerated holes or with superoxide radical or both species. Therefore, $O_2^{-\bullet}$ radical is the most important active species in the photocatalytic process of CV or phenol by BiO_xCl_y/BiO_mI_n.

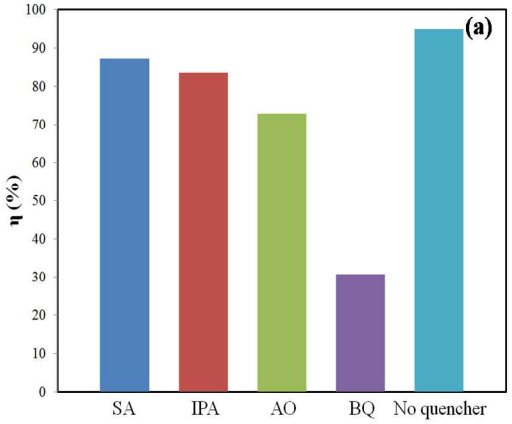

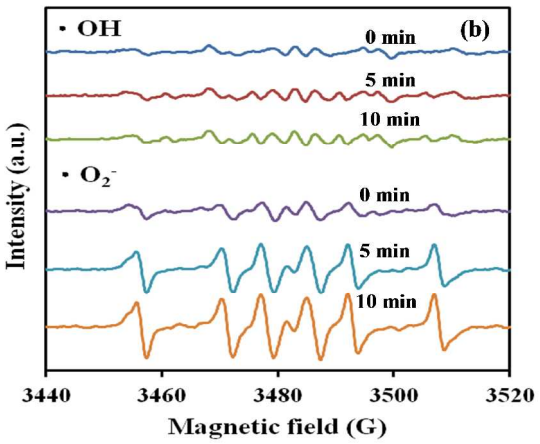

Fig. 10 (a) The dye concentration during photodegradation as a function of irradiation time observed in BiO_pBr_q/BiO_mI_n under the addition of different scavengers: SA, IPA, AQ, and BQ. (b) DMPO spin-trapping EPR spectra for DMPO-O_2^- and DMPO-OH under visible light irradiation with BiO_xCl_y/BiO_mI_n.

Chen *et al.* reported[35] that Pt-TiO_2 accumulated less negative species on catalyst surfaces, which deteriorated reaction rates, than pure TiO_2 did in an acidic environment. The $^{\bullet}OH$ radical is produced subsequently, as also shown in eqs.18-23.

$$O_2^{-\bullet} + H^+ + e^- \rightarrow HOO^{\bullet} \quad (18)$$
$$HOO^{\bullet} + H_2O \rightarrow {}^{\bullet}OH + H_2O_2 \quad (19)$$
$$O_2^{-\bullet} + 2H^+ \rightarrow H_2O_2 \quad (20)$$
$$H_2O_2 + e^- \rightarrow {}^{\bullet}OH + OH^- \quad (21)$$
$$h^+ + OH^- \rightarrow {}^{\bullet}OH \quad (22)$$
$$h^+ + H_2O \rightarrow {}^{\bullet}OH + H^+ \quad (23)$$

These cycles continuously occur when the system is exposed to the visible light irradiation. Finally, after several cycles of photo-oxidation, the degradation of CV by the formed oxidant species can be expressed by eqs. 24-26.

$$CV + h^+ \rightarrow CV^{+\bullet} \rightarrow \text{degraded compounds} \quad (24)$$
$$CV + OH^{\bullet} / O_2^{-\bullet} \rightarrow \text{degraded compounds} \quad (25)$$
$$CV^{+\bullet} + OH^{\bullet} / O_2^{-\bullet} \rightarrow \text{degraded compounds} \quad (26)$$

It has been reported that dye exhibits a mechanisms of dye sensitized degradation.[36] This photocatalytic degradation is also attributed to the photodegradation of CV through the photocatalytic pathway of CV photosensitized BiO_pBr_q/BiO_mI_n. CV absorbing a visible photon is promoted to an excited electronic state CV*, from which an electron can be transferred into the conduction band of BiO_pBr_q/BiO_mI_n:

$$CV + h\nu \rightarrow CV^* \quad (27)$$
$$CV^* + BiO_pBr_q/BiO_mI_n \rightarrow CV^{+\bullet} + BiO_pBr_q/BiO_mI_n\,(e^-) \quad (28)$$
$$O_2 + e^- \rightarrow O_2^{-\bullet} \quad (29)$$

Once the electron reaches the BiO_pBr_q/BiO_mI_n conduction band, it subsequently induces the generation of active oxygen species (eq.29 and eqs.18-21), which result in the degradation of CV. Clearly, apart from the photodegradation of CV through the pathway of BiO_pBr_q/BiO_mI_n-mediated and photosensitized processes, there is another kind of photocatalytic pathway to account for the enhanced photocatalytic activity. Both the photocatalytic process and the photosensitized process would work concurrently, shown in Fig. 11.

In earlier reports,[5,35,37-40] the *N*-de-alkylation processes were preceded by the formation of a nitrogen-centered radical while the destruction of dye chromophore structures was preceded by the generation of a carbon-centered radical in the photocatalytic degradation of Triphenylmethane dye. On the basis of above experimental results, the dye degradation mechanism is tentatively proposed, depicted in Fig. S17-S19 (ESI†).

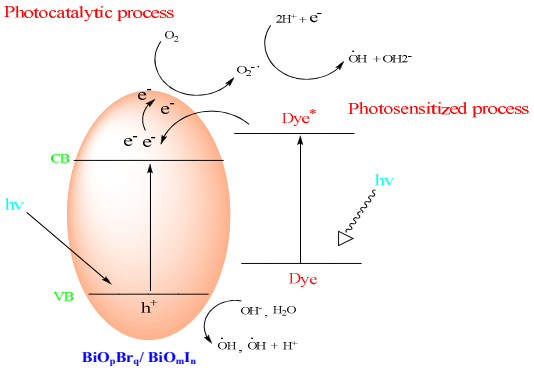

Fig. 11 The band structure diagram of BiO_pBr_q/BiO_mI_n nanocomposites and the possibile charge separation processes.

4. Conclusions

In the current process, the controllable crystal phases and morphologies of bismuth oxybromides/bismuth oxyiodides could be accomplished by simply changing some growth parameters, including molar ratio (Br/I), pH value, and reaction temperature. The increased photocatalytic activities of BiO_pBr_q/BiO_mI_n could be attributed to the formation of the heterojunction between BiO_pBr_q and BiO_mI_n, which effectively suppresses the recombination of photoinduced electron-hole pairs. Both the photocatalytic process and the photosensitized process would work concurrently. $O_2^{-\bullet}$ is main active species and h^+, $^{\bullet}OH$ two minor active species in

the whole process while $^1O_2$ can be negligible. The reaction mechanisms for Vis/BiO_pBr_q/BiO_mI_n proposed in this study should offer some insight for the future development of technology applications to the degradation of dyes.

Acknowledgements

This research was supported by the Ministry of Science and Technology of the Republic of China (NSC-101-2113-M-142-001-MY3).

Notes and references

1 C. J. Brinker, B. Cornils and M. Bonet, Triarylmethane and Diarylmethane Dyes, 6th Ed., Wiley-VCH, New York, 2001.
2 L. M. Lewis and G. L. Indig, J. Photochem. Photobiol. B: Biolog., 2002, **67**, 139-148.
3 B. P. Cho, T. Yang, L. R. Blankenship, J. D. Moody, M. Churchwell, F. A. Bebland and S. J. Culp, Chem. Res. Toxicol, 2003, **16**, 285-294.
4 K. Yu, S. G. Yang, C. Liu, H. Chen, H. Li, C. Sun and A. B. Stephen, Sci. Technol., 2012, **46**, 7318-7326.
5 Y. H. Liao, J. X. Wang, J. S. Lin, W. H. Chung, W. Y. Lin and C. C. Chen, Catal. Today, 2011, **174**, 148-159.
6 Y. Zhang, N. Zhang, Z.R. Tang and Y.J. Xu, Chem. Sci., 2012, **3**, 2812-2822.
7 M.Q. Yang, Y. Zhang, N. Zhang, Z.R. Tang and Y.J. Xu, Sci. Rep. 2013, 3, 3314.
8. M.Q. Yang, N. Zhang, M. Pagliaro and Y.J. Xu, Chem. Soc. Rev., 2014, **43**, 8240-8254.
9. N. Zhang, Y. Zhang and Yi-Jun Xu, Nanoscale, 2012, 4, 5792–5813.
10 N. Zhang, M.Q. Yang, Z.R. Tang, and Y.J. Xu, ACS Nano, 2014, 8, 623-633.
11 Y. Zhang, Z.R. Tang, X. Fu, and Y.J. Xu, ACS Nano, 2010, 4, 7303-7311.
12 C. Han, M.Q. Yang, B. Weng and Y.J. Xu, Phys. Chem. Chem. Phys., 2014, 16, 16891-16903.
13 W. W. Lee, C. Lu, C. Chuang, Y. Chen, J. Fu, C. Siao and C. Chen, RSC Adv., 2015, DOI: 10.1039/C4RA15072D.
14 L. Ye, J. Chen, L. Tian, J. Liu, T. Peng, K. Deng and L. Zan, Appl. Catal. B: Environ., 2013, **130-131**,1-7.
15 Y. R. Jiang, H. P. Lin, W. H. Chung, Y. M. Dai, W. Y. Lin, C. C. Chen, J. Hazard. Mater., 2015**, 283**, 787-805
16 S. T. Huang, Y. R. Jiang, S. Y. Chou, Y. M. Dai and C. C. Chen, J. Mol. Catal. A: Chem., 2014, **391**, 105-120.
17 S. Shenawi-Khalil, V. Uvarov, S. Fronton, I. Popov and Y. Sasson, Appl. Catal. B: Environ., 2012, **117-118**, 148-155.
18 X. Xiao, R. Hao, M. Liang, X. Zuo, J. Nan, L. Li and W. Zhang, J. Hazard. Mater., 2012, **233-234**, 122-130.
19 J. Cao, B. Xu, B. Luo, H. Lin and S. Chen, Catal. Commun., 2011, **13**, 63-68.
20 X. Xiao, R. Hao, X. Zuo, J. Nan, L. Li and W. Zhang, Chem. Eng. J., 2012, **209**, 293–300.
21 X. Xiao and W.D. Zhang, RSC Advances, 2011, **1**, 1099–1105.
22 J. Zhang, F. Shi, J. Lin, D. Chen, J. Gao, Z. Huang, X. Ding and C. Tang, Chem. Mater., 2008, **20**, 2937-2941.
23 J. Wang, Y. Yu and L. Zhang, App. Catal. B: Environ., 2013, **136-137**, 112-121.
24 W. D. Wang, F. Q. Huang and X. P. Lin, Scr. Mater., 2007, **56**, 669-672.
25 C. Nasr, K. Vinodgopal, L. Fisher, S. Hotchandani, A. K. Chattopadhyay and P.V.J. Kamat, Phys. Chem., 1996, **100**, 8436-8442.
26 X. Xiao, R. Hu, C. Liu, C. Xing, X. Zuo, J. Nan and L. Wang, Chem. Eng. J., 2013, **225**, 790-797.
27 S. K. Sana, U. Vladimir, F. Sveta, P. Inna and S. Yoel, Appl. Catal. B: Environ., 2012, **117-118,** 148-155.
28 L. Chen, S. F. Yin, S. L. Luo, R. Huang, Q. Zhang, T. Hong and P. C. T. Au, Ind. Eng. Chem. Res., 2012, **51**, 6760-6768.
29 J. Wang, Y. Yu and L. Zhang, Appl. Catal. B: Environ., 2013, **136-137**, 112-121.
30 M. C. Yin, Z. S. Li, J. H. Kou and Z. G. Zou, Environ. Sci. Technol., 2009, **43**, 8361-8366.
31 L. S. Zhang, K. H. Wong, H. Y. Yip, C. Hu, J. C. Yu, C. Y. Chan and P. K. Wong, Environ. Sci. Technol., 2010, **44**, 1392-1398.
32 S. G. Meng, D. Z. Li, M. Sun, W. J. Li, J. X. Wang, J. Chen, X. Z. Fu and G. C. Xiao, Catal. Commun., 2011, **12**, 972-975.
33 G. Li, K. H. Wong, X. Zhang, C. Hu, J. C. Yu, R. C. Y. Chan and P. K. Wong, Chemosphere, 2009, **76**, 1185-1191.
34 X. Xiao, C. Xing, G. He, X. Zuo, J. Nan and L. Wang, Appl. Catal. B: Environ., 2014, **148–149**, 154–163.
35 H. J. Fan, C. S. Lu, W. L. W. Lee, M. R. Chiou and C. C. Chen, J. Hazard. Mater., 2011, **185**, 227-235.
36 X. Zhu, J. Zhang and F. Chen, Appl. Catal. B: Environ., 2011, **102**, 316-322.
37 H. P. Lin, J. Y. Chen, W. H. Lien and C. C. Chen, J. Taiwan Inst. Chem. Eng., 2014, **45**, 2469-2479.
38 K. L. Li, W. W. Lee, C. S. Lu, Y. M. Dai, S. Y. Chou, M. C. Wang and C. C. Chen, J. Taiwan Inst. Chem. Eng., 2014, **45**, 2688-2697.
39 H. L. Chen, W. W. Lee, W. H. Chung, Y. J. Chen, Y. R. Jiang, H. P. Lin, W. Y. Lin and C. C. Chen, J. Taiwan Inst. Chem. Eng., 2014, **45**, 1892-1909.

40 W. W. Lee, C. S. Lu, C. W. Chuang, Y. J. Chen, J. Y. Fu, C. W. Siao, C. C. Chen, RSC Advances, 2015**, 5**, 23450–23463.

